A PEGylation-Free Biomimetic Porphyrin Nanoplatform for Personalized Cancer Theranostics

Liyang Cui,[†,‡,§] Qiaoya Lin,[†,⊥] Cheng S. Jin,[†,∥,#] Wenlei Jiang,[†] Huang Huang,[†] Lili Ding,[†] Nidal Muhanna,[†,▽] Jonathan C. Irish,[†,▽] Fan Wang,[§] Juan Chen,[*,†] and Gang Zheng[*,†,‡,∥,#]

[†]Princess Margaret Cancer Centre and Techna Institute, University Health Network, Toronto, Ontario M5G 2M9, Canada, [‡]Department of Medical Biophysics, University of Toronto, Toronto, Ontario M5S 2J7, Canada, [§]Medical Isotopes Research Center, Peking University, Beijing 100871, China, [⊥]Britton Chance Center for Biomedical Photonics, Wuhan National Laboratory for Optoelectronics, Huazhong University of Science & Technology, Wuhan 430074, China, [∥]Department of Pharmaceutical Sciences, Leslie Dan Faculty of Pharmacy, University of Toronto, Toronto, Ontario M5S 2J7, Canada, [#]Institute of Biomaterials and Biomedical Engineering, University of Toronto, Toronto, Ontario M5S 2J7, Canada, and [▽]Otolaryngology — Head and Neck Surgery, University of Toronto, Toronto, Ontario M5S 2J7, Canada

ABSTRACT PEGylation (PEG) is the most commonly adopted strategy to prolong nanoparticles' vascular circulation by mitigating the reticuloendothelial system uptake. However, there remain many concerns in regards to its immunogenicity, targeting efficiency, *etc.*, which inspires pursuit of alternate, non-PEGylated systems. We introduced here a PEG-free, porphyrin-based ultrasmall nanostructure mimicking nature lipoproteins, termed PLP, that integrates multiple imaging and therapeutic functionalities, including positron emission tomography (PET) imaging, near-infrared (NIR) fluorescence imaging and photodynamic therapy (PDT). With an engineered lipoprotein-mimicking structure, PLP is highly stable in the blood circulation, resulting in favorable pharmacokinetics and biodistribution without the need of PEG. The prompt tumor intracellular trafficking of PLP allows for rapid nanostructure dissociation upon tumor accumulation to release monomeric porphyrins to efficiently generate fluorescence and photodynamic reactivity, which are highly silenced in intact PLP, thus providing an activatable mechanism for low-background NIR fluorescence imaging and tumor-selective PDT. Its intrinsic copper-64 labeling feature allows for noninvasive PET imaging of PLP delivery and quantitative assessment of drug distribution. Using a clinically relevant glioblastoma multiforme model, we demonstrated that PLP enabled accurate delineation of tumor from surrounding healthy brain at size less than 1 mm, exhibiting the potential for intraoperative fluorescence-guided surgery and tumor-selective PDT. Furthermore, we demonstrated the general applicability of PLP for sensitive and accurate detection of primary and metastatic tumors in other clinically relevant animal models. Therefore, PLP offers a biomimetic theranostic nanoplatform for pretreatment stratification using PET and NIR fluorescence imaging and for further customized cancer management *via* imaging-guided surgery, PDT, or/and potential chemotherapy.

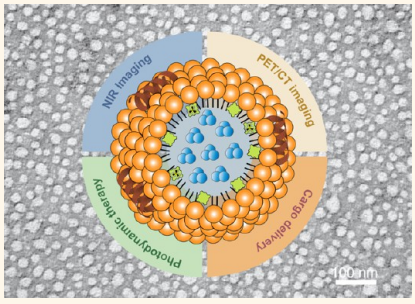

KEYWORDS: porphyrin · nanoparticle · PEGylation · PET imaging · multimodal imaging · fluorescence-guided surgery · photodynamic therapy

Personalized medicine focuses on tailoring of medical treatment to the individual characteristics, needs and preferences of patients during all stages of care from diagnosis, treatment to prognosis. Theranostic, an integrated form of imaging and therapy, plays an increasingly important role in personalized cancer treatment, where imaging modalities not only offer the potential to noninvasively detect and functionally characterize disease, but also provide a quantitative way to assess the delivery of therapy in tumor regions and specify the activation state of a therapeutically shielded drug for finely tuned treatment planning. Furthermore, multimodal imaging could provide complementary information pertaining to the strengths of the individual modalities to better elucidate disease from morphological behaviors to physiological mechanisms. Research in the development of nanoscale theranostics sits at the forefront of rapidly expanding field of cancer personalized medicine to improve solubility of functional agents, protect from premature degradation, prolong blood circulation and enhance tumor accumulation through the enhanced permeability and retention (EPR) effect,[1] and

* Address correspondence to juan.chen@uhnresearch.ca, gang.zheng@uhnres.utoronto.ca.

Received for review February 15, 2015 and accepted April 1, 2015.

Published online April 01, 2015
10.1021/acsnano.5b01077

control drug release.[2] The majority of reported multifunctional nanoparticles, including inorganic,[3−9] organic,[10−13] and the recently reported porphysome,[14] require PEG to ameliorate the stability and avoid fast clearance by reticuloendothelial system (RES) *in vivo*. Although multiple PEGylated nanoparticles have been clinically approved, there remain several concerns including "PEG dilemma" (inhibition of intracellular trafficking of nanoparticles and subsequent endosomal escape),[15−18] immunogenicity,[19,20] anti-PEG immune response,[15,21−23] biocompatibility and toxicity issues following chronic administration.[24,25] Previous attempts to solve the issues typically involve developing PEG linker-removable approaches,[26] using nonbioadhesive surface-coating materials, such as polysaccharides, poly(vinyl alcohol), and other nonbioadhesive hydrophilic polymers,[27] or hitchhiking blood cells to prolong intravascular particle circulation.[28] Lipoproteins are naturally existing nanoparticles that evade RES uptake, thus exhibiting a long circulating half-life (the native HDLs in humans have a circulating half-life of 9−15 h[29]), offering another PEG-free pathway to design biomimetic long circulating theranostic nanomedicine.[30−39] By engaging the biocompatible nanostructure of lipoprotein and the multifunctionalities of naturally derived porphyrin molecules, we developed a novel PEG-free, porphyrin-based ultrasmall nanostructure mimicking nature lipoproteins, termed porphylipoprotein (PLP), which contains a hydrophobic drug-loadable core, enveloped in porphyrin-lipid monolayer, and constrained by ApoA-1 mimetic R4F (Ac-FAEKFKEAVKDYFAKFWD) peptide networks. We demonstrated that the α-helix structure endorsed by peptide network played an essential role in constricting the size, stabilizing the particles, and the favorable pharmacokinetic behaviors *in vivo* without need of PEG. PLP nanoplatform integrates a variety of imaging and therapeutic functionalities including positron emission tomography (PET) imaging, activatable near-infrared (NIR) fluorescence and photodynamic therapy (PDT). More importantly, we demonstrated that PLP potentiated the customized cancer management on a clinically relevant glioblastoma multiforme (GBM) model. The tumor-selective activation of NIR fluorescence facilitated the delineation of tumor, providing real-time low-background intraoperative guidance for complete tumor resection. Consistently, the selectively activated photodynamic reactivity enabled potent PDT for tumor ablation and surgery bed cleaning. The general applicability of PLP for sensitive and accurate detection of primary and metastatic tumors was further demonstrated in other clinically relevant animal models.

RESULTS AND DISCUSSION

Synthesis and Characterization of PLP. PLP was formulated by assembly of porphyrin-lipid and DMPC-phospholipid on a hydrophobic core in aqueous buffered solution, followed by size-constraint with an 18-amino acid ApoA-1 mimetic peptide R4F (Figure 1a). Transmission electronic microscopy (TEM) showed a spherical structure of PLP with 20 nm in diameter (Figure 1b). At the 400 000 magnification view of TEM, a core−shell lipoprotein-mimicking structure of PLP was revealed (Figure1b, top right corner). The size distribution and ζ potential were determined by dynamic light scattering measurement, showing a monodispersed particle peak at 20.6 ± 5.2 nm (Figure S1, Supporting Information) with ζ potential of −6.07 ± 0.71 mV. A fingerprint α-helix structure of PLP was revealed by circular dichroism (CD) spectrum, manifesting the role of peptide on the control of the particle structure (Figure 1c).[40]

The photophysical properties of PLP are dependent on the proportion of porphyrin-lipid in the total phospholipid used for nanoparticle construction. Increasing the content of porphyrin-lipid led to the enhancement of porphyrin fluorescence quenching together with the increase of particle size (Figure S2). The PLP with 30 mol % of porphyrin-lipid was chosen as an optimal formulation given its high-density packing of porphyrin-lipid (fluorescence quenching efficiency >95%, Figure 1e) and favorable size (<30 nm). According to its characteristic absorption bands of porphyrin at peaks of 420 and 680 nm (Figure 1d) and the particle concentration calculated by the previously reported method for lipoprotein-like nanoparticles,[41] the estimated extinction coefficient of PLP was $\varepsilon_{680} = 7.8 \times 10^7$ cm^{-1} M^{-1}, further confirming the highly dense packing of porphyrin-lipid on PLP. Consistent with the fluorescence quenching, the photodynamic reactivity was also suppressed in intact PLP which exhibited 2−3 fold less singlet oxygen generation compared to the nanostructure-disrupted samples at a wide range of light fluence (0.5−10 J/cm^2, Figure 1f). These results suggest that the photoactivity of PLP is "switched-off" in the intact form, but can be promptly "switched-on" upon its structural disruption, thus exhibiting an activatable fashion for low background fluorescence imaging and selective PDT. In addition, taking advantage of the intrinsic metal chelation capacity of porphyrin, PLP can be directly labeled with radionuclide copper-64 through a robust one-pot procedure to attain ^{64}Cu-PLP with high yield (97.5 ± 1.8%, $n = 5$) and high stability (93.8 ± 2.1%, $n = 5$) within 24 h storage (the methods for measuring labeling efficiency and stability are available in the Supporting Information).

Pharmacokinetics of PLP. The α-helix peptide network not only facilitated the constraint of PLP size, but also stabilized the nanostructure under physiological condition. As shown in Figure 1g, PLP remained highly fluorescence-quenched either in stock PBS at 4 °C (98.4%) or in PBS containing 10% FBS at 37 °C (97.0%) for 24 h, indicating insignificant occurrence of particle dissociation. The pharmacokinetic profile of

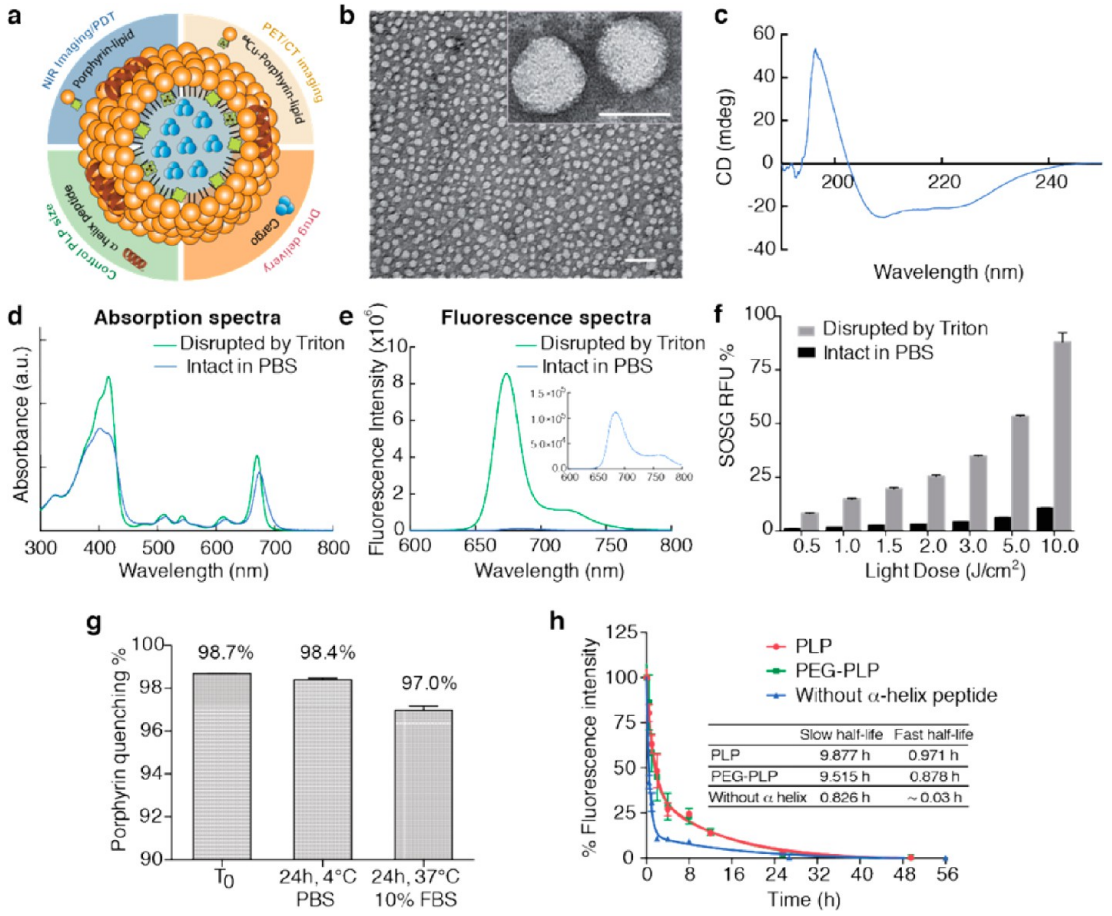

Figure 1. The scheme and characterization of PLP. (a) Schematic of PLP structure. (b) TEM showed a core−shell spherical structure of PLP with size around 20 nm (the scales represented 100 and 20 nm respectively, for the whole view and the magnified view). (c) Circular dichroism spectrum of PLP, affirming the α-helix structure assembled on the particle. (d) UV−vis absorption spectra of intact (blue) and nanostructure-disrupted (green) PLPs. (e) Fluorescence emission spectra of intact (blue) and disrupted (green) PLPs. (f) Singlet oxygen generation of intact and disrupted PLP upon laser irradiation at light dose from 0.5 to 10 J/cm^2 measured by singlet oxygen sensor green (SOSG) assay. (g) Stability of PLP monitored by the change of porphyrin fluorescence quenching efficiency under different condition: the freshly prepared PLP (T_0); the sample stored for 24 h at 4 °C in PBS; and the sample incubated at 37 °C in 10% FBS for 24 h. (h) Blood clearance curve of PLP (red, n =5), PEGylated PLP (green, n =5) and PLP formulation without α-helix (blue n = 4) in mice. The profiles fit into the two-compartment model with slow half-life of 9.88 h for PLP and 9.52 h for PEGylated PLP.

PLP showed a favorable slow half-life (9.9 h) similar to that of PEGylated PLP (containing 5 mol % of PEG-lipid) with half-life of 9.5 h (Figure 1h). However, without the α-helix peptide, the particle dissociated very quickly in the bloodstream showing a slow half-life of 0.83 h only. These results suggested that the α-helix peptide plays a key role in stabilizing nanoparticles to provide PEG-free PLP a favorite circulation time comparable to that of PEGylated PLP, thus excluding the need of PEG for favoring the pharmacokinetics of PLP. Therefore, PLP has confirmed to mimic not only the structure of lipoproteins, but also their biological behaviors to circulate in the bloodstream with a favorite half-life.

Fast Fluorescence and Photodynamic Activation of PLP. Compared with the previously reported liposome-like porphysomes, the PEG-free, ultrasmall, α-helix structured PLP showed significantly enhanced intracellular uptake in cancer cells. As shown in Figure 2a, PLP exhibited 10 times higher uptake than porphysome in U87 cancer cells after 3 h incubation with the same concentration of porphyrin. In addition, unlike the fluorescence activation of porphysome in cell experienced a time-consuming process,[14,42] PLP exhibited rapid activation of porphyrin fluorescence in cells without showing gradual increase of fluorescence after incubation (Figure 2b,c). These data implied that the PLP nanostructure facilitated not only the tumor intracellular uptake, but also fast fluorescence activation.

The *in vivo* behaviors of these two particles were further compared in the SKOV3 orthotopic ovarian cancer model by using their ^{64}Cu-labled versions. As shown in Figure 2d, PLP exhibited very similar biodistribution as PEGylated porphysome, but displayed notably lower spleen uptake than porphysome (3.4 ± 0.2% ID/g *versus* 19.8 ± 1.6% ID/g, n = 3, P < 0.01), fitting to the biodistribution pattern observed for lipoprotein-like nanoparticles.[41] Although the two nanoparticles displayed similar tumor accumulation

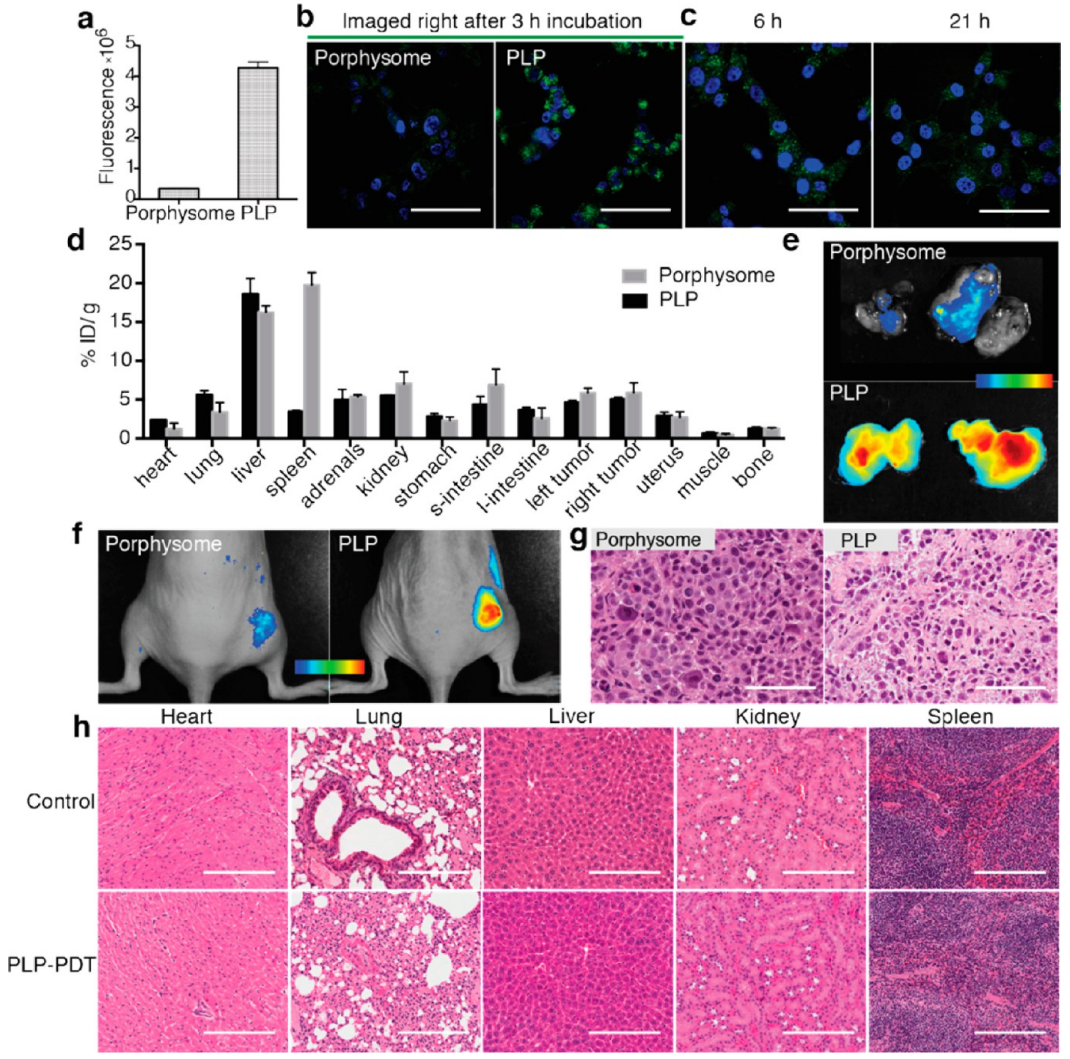

Figure 2. PLP enabled fast activation of fluorescence and photodynamic activity. (a) Comparing the cell uptake of porphysome and PLP in U87 cells by measuring the porphyrin fluorescence of the corresponding cell lysate (n = 3, P < 0.05). (b) Confocal images of U87 cells right after 3 h incubation with porphysome or PLP. (c) Consecutive confocal imaging of the PLP-incubated cells at 6 and 21 h after 3 h incubation. Scale bar in (b) and (c) was 50 μm. (d) Biodistribution of ^{64}Cu-porphysome and ^{64}Cu-PLP in SKOV3 orthotopic ovarian cancer model (n = 3, mean ± SEM) quantified by γ-counting assay. (e) Representative *ex vivo* fluorescence images of the exercised orthotopic SKOV3 tumors from ^{64}Cu-porphysome and ^{64}Cu-PLP porphysome dosed mice, respectively. (f) *In vivo* fluorescence activation of porphysome *versus* PLP in KB-xenograft model at 24 h after intravenous injection. (g) H&E staining of tumor sections at 24 h after porphysome-PDT and PLP−PDT (scale bar: 50 μm). (h) H&E staining of hearts, lungs, livers, kidneys and spleens from mice with or without conducting PLP−PDT treatment (scale bar: 200 μm).

based on γ-counting, PLP exhibited much higher fluorescence in tumor compared to porphysome under *ex vivo* fluorescence imaging (Figure 2e), confirming the rapid fluorescence activation of PLP *in vivo*. We next investigated if the suppressed photodynamic reactivity of PLP could also be quickly activated in tumors. After 24 h administration of PLP or porphysome with the same porphyrin dose, it is unsurprised to find that the KB-xenograft mice administrated with PLP displayed much stronger tumor fluorescence than porphysome-dosed ones (Figure 2f). The fluorescent tumors then received localized laser treatment (671 nm, 100 mW/cm^2, 75 J/cm^2), and the treatment efficacy was examined by H&E histological analysis at 24 h post-PDT. As shown in Figure 2g, PLP−PDT group showed clear tumor cellular damage while porphysome-PDT group gave negligible effect, suggesting that PLP enabled a fast photodynamic activation in tumors for selective and effective PDT. In addition, no obvious cellular damage and morphology change were observed in the healthy organs of PLP−PDT groups compared to blank control (Figure 2h), indicating that the PLP−PDT is a safe treatment approach.

Theranostics Application of PLP for GBM Management. Efficient delivery of imaging and therapeutic agents into intracerebral region remains a major challenge in GBM management. Conventional therapeutic agents are often blocked by the blood-brain barrier (BBB) and

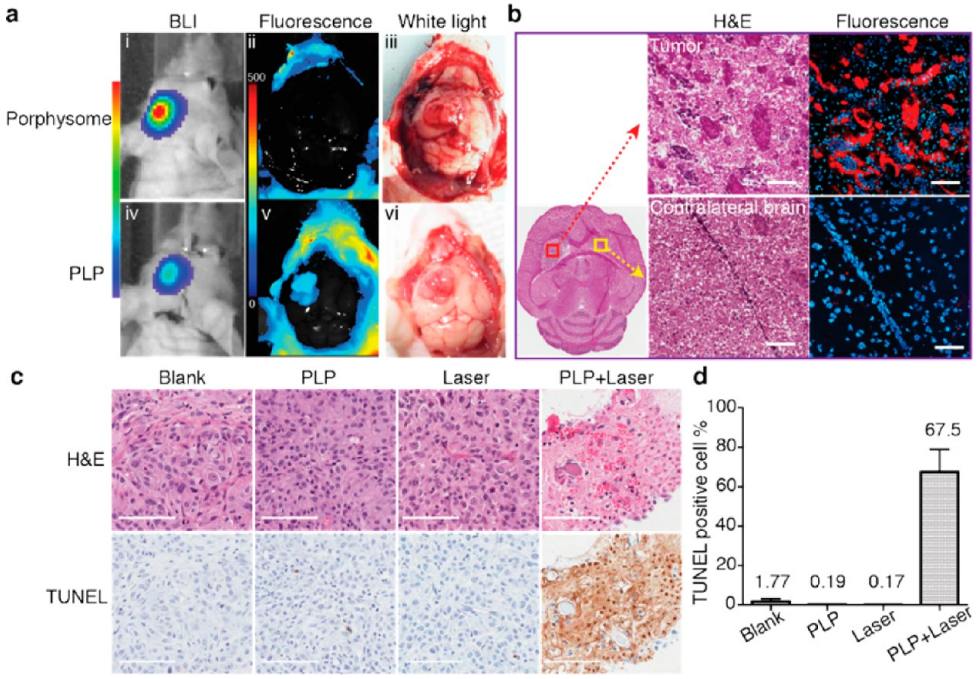

Figure 3. Tumor-specific accumulation and PDT activation of PLP in glioma. (a) Intraoperative bioluminescence, fluorescence and white light images of 9L^{luc} glioma-bearing mice under the crania opening after 24 h injection of porphysomes and PLP. (b) Representative H&E staining image of brain from PLP-administrated mice, with the magnified images showed the corresponding H&E staining and fluorescence microscopic imaging (blue: DAPI, red: porphyrin) of the tumor region and contralateral healthy brain region (scale bar: 100 μm). (c) Representative H&E and TUNEL staining of glioma tumor sections from the blank control, laser alone control, PLP alone control and PLP−PDT group at 24 h post-PDT (scale bar: 100 μm). (d) Quantitative analysis of TUNEL positivity out of whole tumor region in the four groups (n = 3).

cannot access to the glioma cells. Even in the BBB-compromised case, other obstacles, such as the brain blood tumor barrier and the dynamic force caused by the cerebrospinal fluid, hinder the effective drug delivery upon systematic administration.[43,44] Here we assessed the theranostic potential of PLP in a clinically relevant GBM model. The results in Figure 3a demonstrated that PLP significantly accumulated in tumor of the 9L^{luc} gliosarcoma mice with high fluorescence of tumor against the nonfluorescent surrounding healthy brain. The detected PLP fluorescence (Figure 3a-v) was well colocalized with the tumor bioluminescence (BLI) signal (Figure 3a-iv) and with the visualized tumor tissue under the crania opened view (Figure 3a-vi). In contrast, porphysome-dosed animals showed negligible tumor fluorescence under the same imaging setting (Figure 3a-ii), demonstrating the superiority of PLP in brain tumor delivery and detection. When comparing fluorescence microscopic imaging and H&E image of the PLP-dosed brain tissue slides, strong porphyrin fluorescence was observed only in tumor region, but not in the contralateral brain (Figure 3b), further validating the tumor specific uptake of PLP.

In observation of significant fluorescence activation of PLP in glioma tumor, we expected efficient PDT activity as well. Four groups, including blank control, laser control, PLP control and PLP−PDT (PLP + Laser) group, were employed to evaluate the PDT efficacy of PLP. At 24 h postinjection, PLP−PDT group was subjected to trans-cranium laser irradiation (671 nm, 50 mW/cm^2, 50 J/cm^2) (a detailed procedure on trans-skull PDT is available in the Supporting Information). Minimal temperature increase during the treatment excluded the thermal effect (Figure S3a). The PDT efficacy was evaluated by *postmortem* histopathological analysis. PLP−PDT group displayed condensed nuclei and loss of cell structure in tumor while control groups did not (Figure 3c). TUNEL staining analysis further revealed that PLP−PDT induced significant tumor cell apoptosis (67.5 ± 11.4%), while the controls showed minimal tumor apoptosis (1.77 ± 1.37% for blank, 0.17 ± 0.05% for laser control and 0.19 ± 0.07% for PLP control) (Figure 3d). Moreover, the adjacent healthy brain after PLP-PDT showed none of cellular damage, morphology change and cell apoptosis (Figure S3b), demonstrating the high selectivity of PLP−PDT to tumors. Therefore, PLP−PDT could be an appealing alternative[45] to current radiation treatment for treating GBM subtypes that are not surgically accessible or for cleaning the surgery bed after operative procedure.[46]

Stable Delivery of PLP into GBM. In observation of rapid fluorescence and photodynamic activation of PLP in GBM, we next experimented to investigate if PLP remained stable during the systemic delivery. The core−shell structure of PLP allowed for loading of a NIR hydrophobic dye, DiR-BOA, in the particle core without compromising the particle structure and optical properties (Figure S4), thus providing a dual

fluorescence labeled PLP (core labeled with DiR-BOA and shell labeled with porphyrin) to track the particle integrity during systemic delivery. The CRI Maestro hyperspectral imaging system equipped with yellow filter (Ex. 575−605 nm, Em: 645−730 nm) and NIR filter (Ex: 725−755 nm, Em: 780 nm long-pass) was used to monitor porphyrin and DiR-BOA fluorescence, respectively. At 24 h post-administration of PLP(DiR-BOA) in orthotopic U87 glioma bearing mice, brain tumor margin was clearly delineated from surrounding healthy brain by both porphyrin and DiR-BOA fluorescence. The remarkable colocalization of two fluorescence signals suggested that PLP maintained integrity during the systemic delivery and allowed for a stable and efficient delivery of both shell and core components into tumor *in vivo* (Figure 4a). Notably, the *ex vivo* tissue fluorescence imaging (Figure S5) further confirmed the well-matched porphyrin and DiR-BOA signals in most of organs, demonstrating the integrity of PLP during the blood circulation within 24 h. Therefore, the observed rapid fluorescence and photodynamic activation of PLP in tumor were likely happened after the entire particles accumulation, excluding the concern of premature degradation of PLP.

PLP for Intraoperative Fluorescence-Guided Surgery of GBM. Surgical removal of the tumors remains the mainstream of GBM treatment prior to other treatments in clinic, but it experienced major challenge on precise delineation positive margins for sufficient surgery while maintaining important neuro-functions.[47,48] PLP demonstrated its stable systemic delivery and its ability for delineation of tumor from surrounding healthy brain by the activated porphyrin fluorescence. Even at microscopic level, it allowed for highly sensitive detection of tumor by an *in vivo* confocal microscopy (Figure 4b), separating completely from the nonfluorescent contralateral brain tissue. We therefore investigated PLP as fluorescent intraoperative guide for brain tumor surgery. Orthotopic $U87^{GFP}$ glioma mice with tumor deeply seeded inside brain (over 5 mm deep from top surface, identified by MRI in Figure 4c-ii) were used to mimic clinical scenario. At 24 h after injection of PLP(DiR-BOA), both intrinsic porphyrin fluorescence and DiR-BOA fluorescence could be detected by fluorescence molecular tomography (FMT) imaging system in glioma mice (Figure 4c-iii), while neither was detected in the brain of sham control (mice received the same surgical procedure as the glioma mice but had saline injection instead of tumor cells) (Figure S6), eliminating the possibility of false-positive uptake of PLP related to tumor-induction surgery. As illustrated in Figure 4d, the brain was subjected to the coronal transection to remove the top portion with minimal malignancy (negligible GFP signal of tumor) and to expose the major solid tumor (strong GFP signal of tumor) in the bottom portion. The tumor and malignant peripheral region were clearly delineated by both porphyrin and DiR-BOA fluorescence and the two signals were well-correlated with the tumor GFP signal (Figure 4e). Guided with the porphyrin fluorescence, the suspicious malignancy was surgically removed and the final surgery bed exhibited minimal porphyrin and GFP fluorescence, implying the completion of tumor resection. The resected tissues were confirmed malignant by histological analysis and displayed the well-matched porphyrin fluorescence and tumor GFP signal under fluorescence microscopy (Figure S7), indicating that PLP was able to detect primary tumor at cellular level to precisely guide the surgery. Malignant gliomas sometimes occur within multiple compartments in the brain and lead to the failure in the gross total resection.[49] PLP demonstrated the ability to identify multiple foci of $U87^{luc}$ tumors that scattered through the mice brain ranging from 4 mm to less than 1 mm in size with matched porphyrin fluorescence and tumor BLI signal (Figure 4f). Given that surgical outcome is critical for GBM management and prognosis, PLP fluorescence-guided tumor dissection presented a promising add-on to facilitate the standard surgery procedure.

Multimodal Imaging Application of PLP on Other Cancer Models. Beyond the GBM application, we further evaluated the theranostic applicability of PLP in other types of primary and metastatic tumor animal models. After 24 h injection of ^{64}Cu-PLP with the radioactivity of 43 Ci per μmol of particle, the deep-seated PC-3 orthotopic prostate tumor was clearly delineated in both axial and coronal views of coregistered PET and computed tomography (CT) images (Figure 5a). The tumor-selective accumulation was quantitatively confirmed by γ-counting assay, which revealed significantly higher PLP accumulation in tumor (5.27 $\pm$ 0.48% ID/g) *versus* healthy prostate (1.95 $\pm$ 0.81% ID/g) (n = 4, P < 0.05, Figure 5b). Meantime, significantly higher fluorescence was observed in tumor over the surrounding organs (Figure 5c) under *ex vivo* tissue imaging. On the basis of the high fluorescence contrast of tumor/nontumor, nonradioactive PLP was then explored for fluorescence-guided intervention of primary prostate tumor. At 24 h postinjection of 10 mg/kg of PLP, the orthotopic tumor was depicted noninvasively by imaging coregistration of CT and FMT, suggesting that the activated inherent fluorescence of PLP enabled preoperative assessment of prostate orthotopic tumor (Figure 5d). The fluorescent region under FMT/CT view was surgically exposed and the tumor in pelvic cavity was clearly demarcated under intraoperative fluorescence imaging (Figure 5e-i). Guided with the porphyrin fluorescence, the suspicious tumor tissue was resected. The clean surgical bed (Figure 5e-ii) after tumor removal validated the tumor-preferential accumulation and activation of PLP.

The multimodal cancer imaging by PLP was further evaluated in a luciferase-expressing metastatic tumor

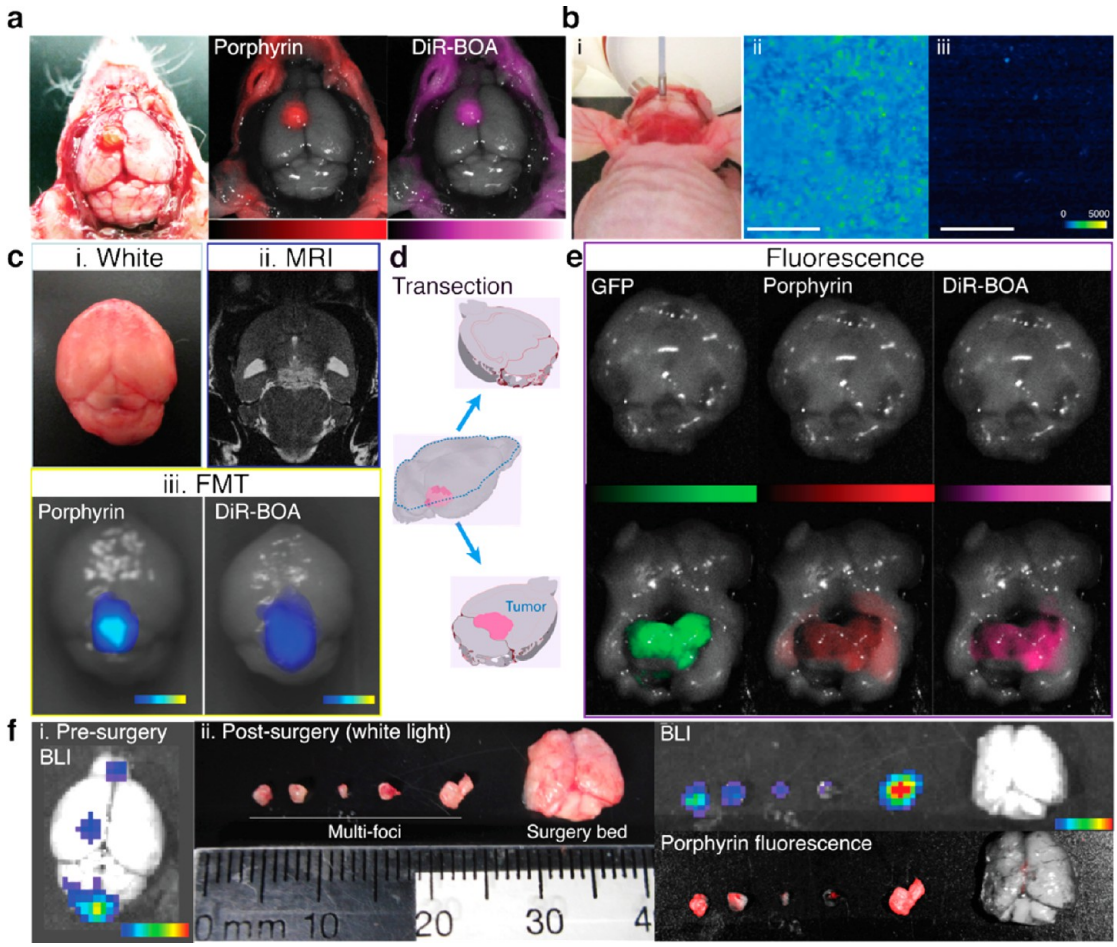

Figure 4. Image-guided intervention of glioblastoma multiforme by PLP. (a) Photograph image and the corresponding porphyrin and DiR-BOA fluorescence images of the brain from the orthotopic U87^{GFP} glioma mice at 24 h post-injection of PLP(DiR-BOA). (b) Representative *in vivo* fluorescence microscopic images of tumor (ii) and contralateral brain (iii) obtained with deep red long-pass laser probe (i) under the crania opening (the scales in both b(ii) and b(iii) are 100 μm). (c) The entire brains with deep-seeded U87^{GFP} tumor were imaged by photograph image (i); MRI (ii); and FMT (iii) at 24 h postinjection of PLP(DiR-BOA). Followed the transection procedure illustrated in (d), the two separated portions were subjected to CRI Maestro hyperspectral imaging system to detect GFP signal (tumor cells), porphyrin signal (PLP), and DiR-BOA signal (cargo) (e). (f) Multifoci glioma detected by PLP. (i) Bioluminescence image of the entire U87^{luc} tumor-bearing brain. (ii) Photography, bioluminescence and porphyrin fluorescence images of multifoci resection.

model. As shown in Figure 6a, two bright hot spots were detected clearly against the low-background abdomen by ^{64}Cu-PLP enabled PET/CT imaging. The suspicious metastatic ovaries, uterus and muscle were then harvested for *ex vivo* BLI and fluorescence imaging. As shown in Figure 6b, the metastatic tumor displayed strong and well-correlated fluorescence and BLI signals whereas the muscle and connective healthy uterus showed negligible signal. The regions displayed all three signals (radioactivity, fluorescence and BLI) were further confirmed metastasis through both histopathological analysis that showed cancer cell morphology (*e.g.*, enlarged nuclei, prominent nucleoli and irregular shape), and high positive pan-cytokeratin staining (PanCK) that indicated the presence of carcinoma (Figure 6c). Therefore, PLP could specifically accumulate in both primary and metastatic tumors. This selectivity together with the intrinsic multimodal imaging capacities makes PLP an ideal tracer for tumor diagnosis and image-guided interventions.

Inspired by the nature's nanoparticles, lipoproteins, PLP opens a new avenue for designing PEG-free nanomedicine. The α-helical peptide networks not only enable stable assembly of the multifunctional components within an ultrasmall sized structure, but also render prolonged pharmacokinetic profile, favorable biodistribution, and superior intracellular trafficking. The built-in porphyrin assembly offers the coalition of multiple imaging and therapeutic functions. The natural metal chelating property of porphyrin makes PLP versatile for nuclear medicine. The intrinsic copper-64 labeling allows for noninvasive tracking PLP delivery and essentially accurate and sensitive detection of both primary tumor and metastasis by PET/CT imaging. Other metal ions, such as paramagnetic Mn or Pd, could also be incorporated into porphyrin molecules to provide an additional MRI contrast or to enhance

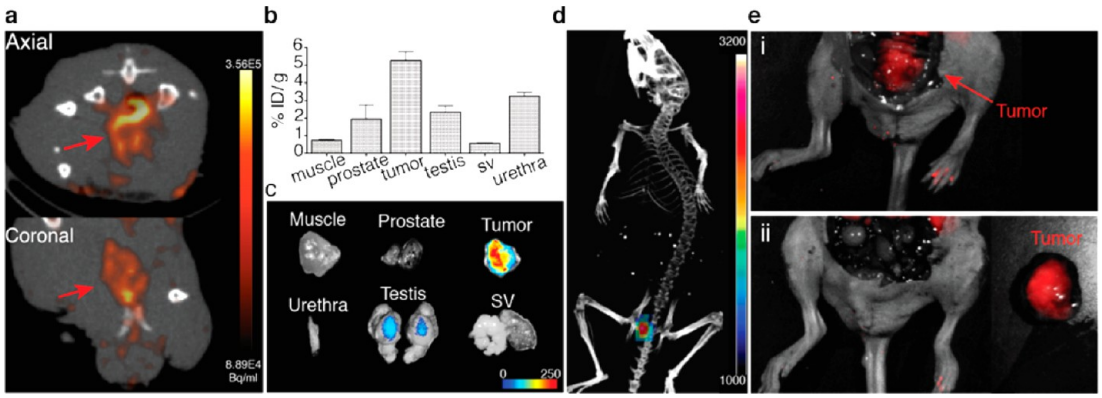

Figure 5. Tumor-specific uptake and multimodal imaging of PLP in orthotopic prostate cancer model. (a) Representative axial and coronal views of PET/CT imaging of PC-3 orthotopic prostate cancer mice after 24 h intravenous injection of ^{64}Cu-PLP (red arrow: tumor). (b) Distribution of ^{64}Cu-PLP in tumor and surrounding tissues calculated as percentage of the injected dose per gram (% ID/g), sv stands for seminal vesicle (n = 4, P < 0.05). (c) *Ex vivo* fluorescence imaging of resected tumor and surrounding tissues. (d) Representative coregistration of CT and fluorescence molecular tomography (FMT) in the region of interest after 24 h intravenous injection of PLP, clearly revealing the tumor margin. (e) Intraoperative fluorescence imaging enabling the guidance of PC-3 orthotopic tumor resection: (i) before and (ii) after resection.

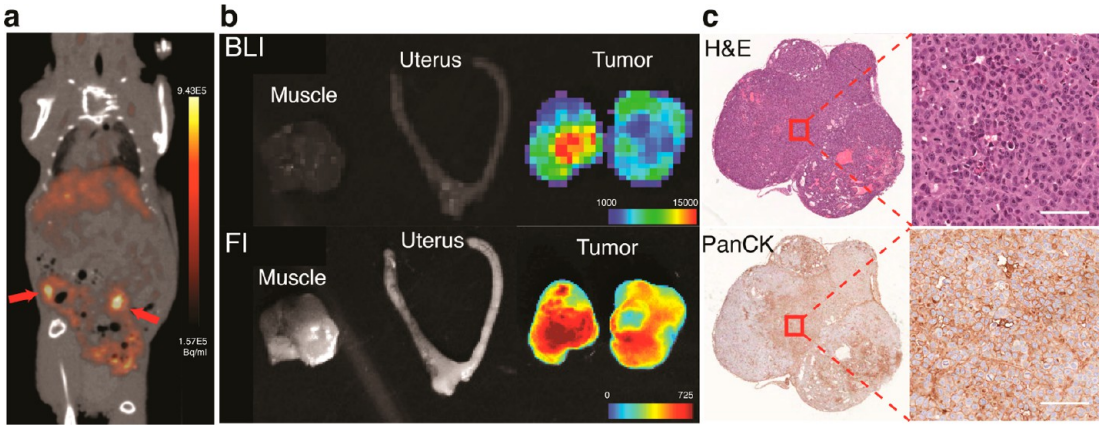

Figure 6. Ovarian cancer metastasis detected by ^{64}Cu-PLP. (a) Representative whole-body PET/CT image of mouse with ovarian cancer metastasis after 24 h intravenous injection of ^{64}Cu-PLP (red arrow: tumor). (b) *Ex vivo* bioluminescence imaging (BLI) and fluorescence imaging (FI) of metastatic tumors, uterus and muscle. (c) The PLP-detected metastases were affirmed by histopathological analysis, showing cancer cell morphology in H&E staining and pan-cytokeratin (PanCK)-positive, (the scale bar in the magnified image: 100 μm).

PDT treatment.[50] The superior PLP intracellular trafficking results in rapid and efficient activation of porphyrin fluorescence and photodynamic reactivity that were both inhibited in intact PLP, thus exhibiting an activatable mechanism for low background fluorescence imaging and tumor-selective PDT. Moreover, the core−shell lipoprotein-mimicking structure of PLP may provide amiable environment for stable delivery of drugs, such as siRNA[51−54] and hydrophobic chemotherapeutics[55−57] for personalized treatment or as adjuvant therapy for synergistic treatment. It should be noted that PLP is distinctively different from our previously reported porphysome in its nanostructure (20 nm *versus* 100 nm, monolayer *versus* bilayer, hydrophobic core *versus* aqueous core, α-helical peptide *versus* PEG coating) and nanostructure-dependent functions (fast *versus* slow intracellular trafficking, photodynamic therapy *versus* photothermal therapy).[14,58]

Although nanosized theranostics exhibits preferential accumulation in malignant tumors through the EPR effect, most of them experience hindrance to sufficient penetration within tumor. Recent studies have demonstrated that nanoparticles with size less than 40 nm was advantageous over larger-sized nanoparticles in efficient penetration into the tumor types that are poorly permeable and highly fibrotic or desmoplastic.[59−61] The PLP owns a favorable size (∼20 nm) for circumvention of fast elimination by kidneys[62] (>5 nm) and for superior diffusion through the tumor interstitium (<40 nm), thus holding great potential for improving drug delivery, especially in tumors with low permeability, such as pancreatic cancer. Though PLP (∼20 nm) and larger-sized porphysome (∼100 nm) exhibited similar tumor accumulation in the SKOV3 orthotopic tumor (Figure 2d), a significant difference was observed for their porphyrin photoreactivity activation (Figure 2e), which indicated that

the small size of PLP might promote its intratumoral transportation, along with its enhanced intracellular trafficking (Figure 2a), leading to sufficient and active porphyrin concentration in tumor cell for high-contrast fluorescence imaging and potent PDT.

Nanotoxicity is one of the general concerns in translation of nanoparticles into clinical practice.[63] Due to the natural chlorophyll origin, porphyrin-based nanoparticles were found biocompatible and biodegradable and had minimal toxicity *in vivo*.[14] Lipoproteins are naturally endogenous protein−lipid nanocomplexes essential for the regulation of lipid metabolism and cholesterol transportation.[64] Lipoprotein-mimicking nanoplatform has been demonstrated with minimal acute toxicity at a dose up to 2000 mg/kg.[56] By engaging the biocompatible nanostructure of lipoprotein and the multifunctional porphyrin molecules, PLP is able to fulfill "the one particle to rule them all" strategy for personalized medicine, sparing from the complexity, immunogenicity and toxicity issues caused by simple piling of different functional moieties. Indeed, PLP administration and PLP−PDT caused no detectable functional or histological side effects on normal tissues. The intrinsic multimodal and biomimetic nature of PLP confers high potential for cancer theranostics and clinical translation.

CONCLUSIONS

The PEG-free lipoprotein-mimicking structure of PLP conferred great biocompatibility and *in vivo* behaviors. With the built-in porphyrin, PLP exhibited intrinsically multimodal imaging and therapeutic functionalities. The inherent activatable NIR fluorescence and metal chelation enabled PET imaging provided comprehensive information for early diagnosis, disease staging, intraoperative guidance, and quantitative assessment of drug delivery. Together with the potent PDT competency, PLP allowed for the tuning of patient treatment *via* imaging-guided surgery and effective PDT.

METHODS

Materials. 1,2-Dimyristoyl-*sn*-glycero-3-phosphocholine (DMPC) was purchased from Avanti Polar Lipids Inc. (AL, USA). Cholesteryl oleate was obtained from Sigma-Aldrich Co. (MO, USA). 1,1′-Dioctadecyl-3,3,3′,3′-tetramethylindotricarbocyanine iodide bis-oleate (DiR-BOA) and the (*Z*)-octadec-9-enyl 2-(3-((*Z*)-octadec-9-enyloxy)-6-oxo-6*H*-xanthen-9-yl) benzoate was synthesized by the previously reported methods.[32] The ApoA-1 mimetic R4F peptide, Ac-FAEKFKEAVKDYFAKFWD, was purchased from GL Biochem Ltd. (Shanghai, China). Porphyrin-lipid was synthesized by the previously reported methods.[14]

PLP Preparation and Characterization. PLP lipid film consists of 0.9 μmol porphyrin-lipid, 2.1 μmol DMPC and 0.3 μmol cholesteryl oleate was prepared under a stream of nitrogen gas. For DiR-BOA-loaded particles, a 3 mol % DiR-BOA was included in the lipid film. For PEGylated PLP formulation, 5 mol % DSPE-PEG_{2000} was added in the lipid film preparation. The completely dried lipid films were hydrated with 1.0 mL of PBS buffer (150 mM, pH 7.5) and sonicated using Bioruptor at low frequency (30 kHz) for 30 cycles (30 s on/30 s off) at 40 °C. R4F peptide (2.3 mg) in 1 mL of PBS was then added into the rehydrated solution and the mixture was kept shaking at 4 °C overnight. The solution was centrifuged at 12 000 rpm for 20 min subsequently and filtered with 0.1 μm membrane (Millex, Sigma-Aldrich). ^{64}Cu-PLP was synthesized using the method reported previously.[65] Briefly, PLP was 1:1 diluted with 0.1 M NH_4OAC buffer (pH 5.5), and then mixed with $^{64}CuCl_2$ solution and incubating at 37 °C for 60 min. Small aliquot of the mixture was purified with the centrifugal units (30K, Amicon Ultra) and the radiochemical purity and yield were assessed.

The prepared PLP was subjected to TEM scanning and dynamic light scattering measurement to determine the particle morphology and size distribution. In the photoproperties measurement, PLP was diluted in either PBS (intact particles) or PBS containing 0.5% Triton X-100 (nanostructure disrupted sample), and subjected to the circular dichroism spectrum, absorption spectra and fluorescence spectrum measurement. Singlet oxygen ($^1O_2$) generation of PLP were measured using singlet oxygen sensor green (SOSG) assay. For the blood clearance study in mice, PLP (n = 5), PEG−PLP (n = 5) and PLP formulation without R4F peptide (n = 4) were intravenously injected to healthy BALB/c mice at the dose of 2.5 mg/kg. Blood was collected prior to and after the injection, the fluorescence of the extracted serum was measured, and the porphyrin amount at each time point was then analyzed by Graphpad Prism to calculate half-life of the particles.

Activation of PLP *versus* Porphysome. To compare the cellular uptake of PLP *versus* porphysome, a quantitative cellular uptake study was performed by measuring the porphyrin fluorescence in cell lysate after 3 h incubation. Confocal imaging was also conducted to monitor the porphyrin fluorescence activation over time *in vitro*. To compare the fluorescence activation *in vivo*, SKOV3 tumor-bearing mice (n = 3) were intravenously injected with ^{64}Cu-PLP or ^{64}Cu-porphyroms. At 24 h after injection, the biodistribution was determined by γ-counting and tumors from both sides of the ovaries were harvested and subjected to *ex vivo* fluorescence imaging. To compare the photodynamic activation, KB-xenograft mice received PLP or porphysome injections at a dose of 5 mg/kg (n = 3 for each group) were subjected to laser irradiation (671 nm, 75 J/cm^2) at 24 h postinjection. Temperature increase of tumors during treatment was monitored by an infrared thermal camera. The therapeutic efficacy was investigated by histological analysis.

Theranostic Application of PLP on GBM Model. The accumulation and activation of PLP in glioma mice were investigated on 9L^{luc} gliosarcoma mice and compared with those of porphysomes. Bioluminescence and open-skull fluorescence imaging were acquired at 24 h after injection. To investigate the drug delivery, U87 mice were injected with DiR-BOA loaded PLP, PLP(DiR-BOA), intravenously and subjected to fluorescence imaging. Fluorescence images were performed using CRI Maestro hyperspectral imaging system with the crania opening to acquire porphyrin and DiR-BOA signals, respectively, using the filter pairs of 575−605 nm excitation/645−730 nm emission and 725−755 nm excitation/780 nm long-pass emission. *In vivo* confocal microscopic imaging was further conducted.

To evaluate the competency of PLP for fluorescence-guided surgery, orthotopic U87^{GFP} glioma mice with deep-seeded tumor were administrated with PLP(DiR-BOA) intravenously. The mice were scarified at 24 h postinjection and the entire brains were subjected to FMT imaging. Following the brain transection procedure illustrated in Figure 4d, the two transected portions were subjected to fluorescence imaging using Maestro system to acquire the signal of GFP, porphyrin and DiR-BOA using different filter pairs (the filter pair for tumor GFP signal is 445−490 nm excitation/515−550 nm emission).

For multifoci resection, *ex vivo* bioluminescence imaging and fluorescence imaging were performed on all the resected U87^{luc} tumors and the remained surgery bed of brain.

The PDT efficacy of PLP for glioma treatment was evaluated on the U87^{luc} mice. The mice were categorized into four groups: blank control group, PDT laser alone, PLP injection alone and PLP−PDT (PLP injection plus PDT laser treatment) ($n = 3$ for each group). The PLP was dosed intravenously at 5 mg/kg and the 671 nm laser irradiation was performed at 24 h postinjection in the trans-cranium manner with laser intensity of 50 mW/cm^2 and total light dose of 50 J/cm^2. The therapeutic efficacy was evaluated by histological analysis.

Multimodal Imaging and Biodistribution Studies of ^{64}Cu-PLP in Orthotopic and Metastatic Cancer Mouse Models. To study the specific uptake of PLP in orthotopic cancer, PC-3 orthotopic prostate tumor-bearing mice were injected with ^{64}Cu-PLP and subjected to PET/CT scanning at 24 h postinjection ($n = 5$). Animals were sacrificed after the scanning, tumor and surrounding organs were then harvested and subjected to fluorescence imaging. After the *ex vivo* imaging, organs of interest were weighed and subjected to the radioactivity measurement by γ-counting assay to calculate the PLP distribution as percentage of the injected dose per gram (% ID/g). For FMT/CT imaging, mice received 10 mg/kg of PLP were subjected sequentially to FMT imaging and microCT scanning in the same chamber at 24 h postinjection. The 3D images from FMT and micro-CT were coregistered using Inveon Research Workplace. For metastatic tumor imaging, MT-1^{luc} metastatic mouse model that received ^{64}Cu-PLP injection was subjected to PET/CT scanning at 24 h postinjection. The mice were then scarified, and the metastatic tumor and surrounding tissues were subjected to *ex vivo* bioluminescence and fluorescence imaging. The metastases were further affirmed by histology studies.

Conflict of Interest: The authors declare no competing financial interest.

Acknowledgment. The authors are thankful for funding support from the Canadian Institutes of Health Research, Ontario Institute for Cancer Research, Natural Sciences and Engineering Research Council of Canada, Major International (Regional) Joint Research Project from National Science Foundation of China, US Army Ovarian Cancer Research Program Translational Synergistic Leverage Award, Prostate Cancer Canada, Canada Foundation for Innovation, Princess Margaret Cancer Foundation and the Joey and Toby Tanenbaum/Brazilian Ball Chair in Prostate Cancer Research. L.C., J.C. and G.Z. conceived the project, planned the experiment, interpreted the data and wrote the manuscript. L.C., Q.L. and J.C. developed and characterized the formulations. L.C. and C.S.J. carried out phototherapy procedures and biodistrubtion studies. W.J. and L.D set up animal models and assisted L.C. in the experiments conducted in GBM models. L.C. and H.H. carried out FMT/CT and PET/CT imaging studies. N.M, J.C.I. and F.W. contributed in the manuscript editing.

Supporting Information Available: Method description in details; The size distribution of PLP (Figure S1); The characterization of PLP containing different molar percentage of porphyrin-lipid (Figure S2); The phototoxicity of PLP−PDT treatment to glioma mice (Figure S3); The characterization of the drug loaded PLP(DiR-BOA) (Figure S4); The biodistribution of PLP(DiR-BOA) in glioma tumor and major organs (Figure S5); The uptake of PLP in sham control (Figure S6); The tissue histology analysis after PLP fluorescence-guided glioma tumor resection (Figure S7); Representative MRI images of orthotopic prostate and ovarian cancer model (Figure S8). This material is available free of charge *via* the Internet at http://pubs.acs.org.

REFERENCES AND NOTES

1. Maeda, H.; Wu, J.; Sawa, T.; Matsumura, Y.; Hori, K. Tumor Vascular Permeability and the Epr Effect in Macromolecular Therapeutics: A Review. *J. Controlled Release* **2000**, *65*, 271–284.
2. Liu, J.; Bu, W.; Pan, L.; Shi, J. NiR-Triggered Anticancer Drug Delivery by Upconverting Nanoparticles with Integrated Azobenzene-Modified Mesoporous Silica. *Angew. Chem., Int. Ed. Engl.* **2013**, *52*, 4375–4379.
3. Xie, J.; Xu, C.; Kohler, N.; Hou, Y.; Sun, S. Controlled Pegylation of Monodisperse Fe_3O_4 Nanoparticles for Reduced Non-Specific Uptake by Macrophage Cells. *Adv. Mater.* **2007**, *19*, 3163–3166.
4. Wuelfing, W. P.; Gross, S. M.; Miles, D. T.; Murray, R. W. Nanometer Gold Clusters Protected by Surface-Bound Monolayers of Thiolated Poly(Ethylene Glycol) Polymer Electrolyte. *J. Am. Chem. Soc.* **1998**, *120*, 12696–12697.
5. Maltzahn, G.; Park, J.; Agrawal, A.; Bandaru, N. K.; Das, S. K.; Sailor, M. J.; Bhatia, S. N. Computationally Guided Photothermal Tumor Therapy Using Long-Circulating Gold Nanorod Antennas. *Cancer Res.* **2009**, *69*, 3892–3900.
6. Qian, X.; Peng, X.; Ansari, D. O.; Yin-Goen, Q.; Chen, G. Z.; Shin, D. M.; Yang, L.; Young, A. N.; Wang, M. D.; Nie, S. *In Vivo* Tumor Targeting and Spectroscopic Detection with Surface-Enhanced Raman Nanoparticle Tags. *Nat. Biotechnol.* **2008**, *26*, 83–90.
7. Koole, R.; van Schooneveld, M. M.; Hilhorst, J.; Castermans, K.; Cormode, D. P.; Strijkers, G. J.; de Mello Donegá, C.; Vanmaekelbergh, D.; Griffioen, A. W.; Nicolay, K.; *et al.* Paramagnetic Lipid-Coated Silica Nanoparticles with a Fluorescent Quantum Dot Core: A New Contrast Agent Platform for Multimodality Imaging. *Bioconjugate Chem.* **2008**, *19*, 2471–2479.
8. Yoon, T.; Yu, K.; Kim, E.; Kim, J.; Kim, B.; Yun, S.; Sohn, B.; Cho, M.; Lee, J.; Park, S. Specific Targeting, Cell Sorting, and Bioimaging with Smart Magnetic Silica Core−Shell Nanomaterials. *Small* **2006**, *2*, 209–215.
9. Liu, J.; Yu, M.; Ning, X.; Zhou, C.; Yang, S.; Zheng, J. Pegylation and Zwitterionization: Pros and Cons in the Renal Clearance and Tumor Targeting of Near-IR-Emitting Gold Nanoparticles. *Angew. Chem., Int. Ed. Engl.* **2013**, *52*, 12572–12576.
10. Gref, R.; Minamitake, Y.; Peracchia, M. T.; Trubetskoy, V.; Torchilin, V.; Langer, R. Biodegradable Long-Circulating Polymeric Nanospheres. *Science* **1994**, *263*, 1600–1603.
11. Park, J. Liposome-Based Drug Delivery in Breast Cancer Treatment. *Breast Cancer Res.* **2002**, *4*, 95–99.
12. Peracchia, M. T.; Fattal, E.; Desmaële, D.; Besnard, M.; Noël, J. P.; Gomis, J. M.; Appel, M.; d'Angelo, J.; Couvreur, P. Stealth® Pegylated Polycyanoacrylate Nanoparticles for Intravenous Administration and Splenic Targeting. *J. Controlled Release* **1999**, *60*, 121–128.
13. Otsuka, H.; Nagasaki, Y.; Kataoka, K. Pegylated Nanoparticles for Biological and Pharmaceutical Applications. *Adv. Drug Delivery Rev.* **2003**, *55*, 403–419.
14. Lovell, J. F.; Jin, C. S.; Huynh, E.; Jin, H.; Kim, C.; Rubinstein, J. L.; Chan, W. C.; Cao, W.; Wang, L. V.; Zheng, G. Porphysome Nanovesicles Generated by Porphyrin Bilayers for Use as Multimodal Biophotonic Contrast Agents. *Nat. Mater.* **2011**, *10*, 324–332.
15. Amoozgar, Z.; Yeo, Y. Recent Advances in Stealth Coating of Nanoparticle Drug Delivery Systems. *Wiley Interdiscip. Rev.: Nanomed. Nanobiotechnol.* **2012**, *4*, 219–233.
16. Mishra, S.; Webster, P.; Davis, M. E. Pegylation Significantly Affects Cellular Uptake and Intracellular Trafficking of Non-Viral Gene Delivery Particles. *Eur. J. Cell Biol.* **2004**, *83*, 97–111.
17. Hatakeyama, H.; Akita, H.; Harashima, H. A Multifunctional Envelope Type Nano Device (Mend) for Gene Delivery to Tumours Based on the Epr Effect: A Strategy for Overcoming the Peg Dilemma. *Adv. Drug Delivery Rev.* **2011**, *63*, 152–160.
18. Hong, R.; Huang, C.; Tseng, Y.; Pang, V.; Chen, S.; Liu, J.; Chang, F. Direct Comparison of Liposomal Doxorubicin with or without Polyethylene Glycol Coating in C-26 Tumor-Bearing Mice: Is Surface Coating with Polyethylene Glycol Beneficial? *Clin. Cancer Res.* **1999**, *5*, 3645–3652.
19. Moghimi, S. M.; Hamad, I.; Andresen, T. L.; Jørgensen, K.; Szebeni, J. Methylation of the Phosphate Oxygen Moiety of Phospholipid-Methoxy(Polyethylene Glycol) Conjugate

Prevents Pegylated Liposome-Mediated Complement Activation and Anaphylatoxin Production. *FASEB J.* **2006**, *20*, 2591–2593.
20. Hamad, I.; Hunter, A. C.; Szebeni, J.; Moghimi, S. M. Poly-(Ethylene Glycol)s Generate Complement Activation Products in Human Serum through Increased Alternative Pathway Turnover and a MASP-2-Dependent Process. *Mol. Immunol.* **2008**, *46*, 225–232.
21. Ishida, T.; Maeda, R.; Ichihara, M.; Irimura, K.; Kiwada, H. Accelerated Clearance of Pegylated Liposomes in Rats after Repeated Injections. *J. Controlled Release* **2003**, *88*, 35–42.
22. Ishida, T.; Ichihara, M.; Wang, X.; Yamamoto, K.; Kimura, J.; Majima, E.; Kiwada, H. Injection of PEGylated Liposomes in Rats Elicits PEG-Specific Igm, Which Is Responsible for Rapid Elimination of a Second Dose of PEGylated Liposomes. *J. Controlled Release* **2006**, *112*, 15–25.
23. Dams, E. T. M.; Laverman, P.; Oyen, W. J. G.; Storm, G.; Scherphof, G. L.; van der Meer, J. W. M.; Corstens, F. H. M.; Boerman, O. C. Accelerated Blood Clearance and Altered Biodistribution of Repeated Injections of Sterically Stabilized Liposomes. *J. Pharmacol. Exp. Ther.* **2000**, *292*, 1071–1079.
24. Robert, N. J.; Vogel, C. L.; Henderson, I. C.; Sparano, J. A.; Moore, M. R.; Silverman, P.; Overmoyer, B. A.; Shapiro, C. L.; Park, J. W.; Colbern, G. T.; *et al.* The Role of the Liposomal Anthracyclines and Other Systemic Therapies in the Management of Advanced Breast Cancer. *Semin. Oncol.* **2004**, *31*, 106–146.
25. Duncan, R.; Gaspar, R. Nanomedicine(s) under the Microscope. *Mol. Pharmaceutics* **2011**, *8*, 2101–2141.
26. MacEwan, S. R.; Callahan, D. J.; Chilkoti, A. Stimulus-Responsive Macromolecules and Nanoparticles for Cancer Drug Delivery. *Nanomedicine* **2010**, *5*, 793–806.
27. Vllasaliu, D.; Fowler, R.; Stolnik, S. Pegylated Nanomedicines: Recent Progress and Remaining Concerns. *Expert Opin. Drug Delivery* **2014**, *11*, 139–154.
28. Chambers, E.; Mitragotri, S. Prolonged Circulation of Large Polymeric Nanoparticles by Non-Covalent Adsorption on Erythrocytes. *J. Controlled Release* **2004**, *100*, 111–119.
29. Eisenberg, S.; Windmueller, H. G.; Levy, R. I. Metabolic Fate of Rat and Human Lipoprotein Apoproteins in the Rat. *J. Lipid Res.* **1973**, *14*, 446–458.
30. Ng, K. K.; Lovell, J. F.; Zheng, G. Lipoprotein-Inspired Nanoparticles for Cancer Theranostics. *Acc. Chem. Res.* **2011**, *44*, 1105–1113.
31. Corbin, I. R.; Zheng, G. Mimicking Nature's Nanocarrier: Synthetic Low-Density Lipoprotein-Like Nanoparticles for Cancer-Drug Delivery. *Nanomedicine* **2007**, *2*, 375–380.
32. Zhang, Z.; Cao, W.; Jin, H.; Lovell, J. F.; Yang, M.; Ding, L.; Chen, J.; Corbin, I.; Luo, Q.; Zheng, G. Biomimetic Nanocarrier for Direct Cytosolic Drug Delivery. *Angew. Chem., Int. Ed. Engl.* **2009**, *48*, 9171–9175.
33. Cormode, D. P.; Frias, J. C.; Ma, Y.; Chen, W.; Skajaa, T.; Briley-Saebo, K.; Barazza, A.; Williams, K. J.; Mulder, W. J.; Fayad, Z. A.; Fisher, E. A. HDL as a Contrast Agent for Medical Imaging. *Clin. Lipidol.* **2009**, *4*, 493–500.
34. Bricarello, D. A.; Smilowitz, J. T.; Zivkovic, A. M.; German, J. B.; Parikh, A. N. Reconstituted Lipoprotein: A Versatile Class of Biologically-Inspired Nanostructures. *ACS Nano* **2011**, *5*, 42–57.
35. Huang, H.; Cruz, W.; Chen, J.; Zheng, G. Learning from Biology: Synthetic Lipoproteins for Drug Delivery. *Wiley Interdiscip. Rev.: Nanomed. Nanobiotechnol.* **2014**, 10.1002/wnan.1308.
36. Marrache, S.; Dhar, S. Biodegradable Synthetic High-Density Lipoprotein Nanoparticles for Atherosclerosis. *Proc. Natl. Acad. Sci. U. S. A.* **2013**, *110*, 9445–9450.
37. Foit, L.; Giles, F. J.; Gordon, L. I.; Thaxton, C. S. Synthetic High-Density Lipoprotein-Like Nanoparticles for Cancer Therapy. *Expert Rev. Anticancer Ther.* **2015**, *15*, 27–34.
38. Allijn, I. E.; Leong, W.; Tang, J.; Gianella, A.; Mieszawska, A. J.; Fay, F.; Ma, G.; Russell, S.; Callo, C. B.; Gordon, R. E.; *et al.* Gold Nanocrystal Labeling Allows Low-Density Lipoprotein Imaging from the Subcellular to Macroscopic Level. *ACS Nano* **2013**, *7*, 9761–9770.
39. Cormode, D. P.; Skajaa, T.; van Schooneveld, M. M.; Koole, R.; Jarzyna, P.; Lobatto, M. E.; Calcagno, C.; Barazza, A.; Gordon, R. E.; Zanzonico, P.; *et al.* Nanocrystal Core High-Density Lipoproteins: A Multimodality Contrast Agent Platform. *Nano Lett.* **2008**, *8*, 3715–3723.
40. Saxena, V. P.; Wetlaufer, D. B. A New Basis for Interpreting the Circular Dichroic Spectra of Proteins. *Proc. Natl. Acad. Sci. U. S. A.* **1971**, *68*, 969–972.
41. Zhang, Z.; Chen, J.; Ding, L.; Jin, H.; Lovell, J. F.; Corbin, I. R.; Cao, W.; Lo, P. C.; Yang, M.; Tsao, M. S.; *et al.* HDL-Mimicking Peptide-Lipid Nanoparticles with Improved Tumor Targeting. *Small* **2010**, *6*, 430–437.
42. Jin, C. S.; Lovell, J. F.; Chen, J.; Zheng, G. Ablation of Hypoxic Tumors with Dose-Equivalent Photothermal, but Not Photodynamic, Therapy Using a Nanostructured Porphyrin Assembly. *ACS Nano* **2013**, *7*, 2541–2550.
43. Zhan, C.; Lu, W. The Blood-Brain/Tumor Barriers: Challenges and Chances for Malignant Gliomas Targeted Drug Delivery. *Curr. Pharm. Biotechnol.* **2012**, *13*, 2380–2387.
44. Stukel, J. M.; Caplan, M. R. Targeted Drug Delivery for Treatment and Imaging of Glioblastoma Multiforme. *Expert Opin. Drug Delivery* **2009**, *6*, 705–718.
45. Bechet, D.; Mordon, S. R.; Guillemin, F.; Barberi-Heyob, M. A. Photodynamic Therapy of Malignant Brain Tumours: A Complementary Approach to Conventional Therapies. *Cancer Treat. Rev.* **2014**, *40*, 229–241.
46. Muller, P. J.; Wilson, B. C. Photodynamic Therapy of Brain Tumors—a Work in Progress. *Lasers Surg. Med.* **2006**, *38*, 384–389.
47. Wilson, T. A.; Karajannis, M. A.; Harter, D. H. Glioblastoma Multiforme: State of the Art and Future Therapeutics. *Surg. Neurol. Int.* **2014**, *5*, 64.
48. Eyupoglu, I. Y.; Buchfelder, M.; Savaskan, N. E. Surgical Resection of Malignant Gliomas-Role in Optimizing Patient Outcome. *Nat. Rev. Neurol.* **2013**, *9*, 141–151.
49. Hassaneen, W.; Levine, N. B.; Suki, D.; Salaskar, A. L.; de Moura Lima, A.; McCutcheon, I. E.; Prabhu, S. S.; Lang, F. F.; DeMonte, F.; Rao, G.; *et al.* Multiple Craniotomies in the Management of Multifocal and Multicentric Glioblastoma. Clinical Article. *J. Neurosurg.* **2011**, *114*, 576–584.
50. MacDonald, T. D.; Liu, T. W.; Zheng, G. An MRI-Sensitive, Non-Photobleachable Porphysome Photothermal Agent. *Angew. Chem., Int. Ed. Engl.* **2014**, *53*, 6956–6959.
51. Lin, Q.; Chen, J.; Jin, H.; Ng, K. K.; Yang, M.; Cao, W.; Ding, L.; Zhang, Z.; Zheng, G. Efficient Systemic Delivery of Sirna by Using High-Density Lipoprotein-Mimicking Peptide Lipid Nanoparticles. *Nanomedicine* **2012**, *7*, 1813–1825.
52. Lin, Q.; Chen, J.; Zhang, Z.; Zheng, G. Lipid-Based Nanoparticles in the Systemic Delivery of Sirna. *Nanomedicine* **2014**, *9*, 105–120.
53. Shahzad, M. M.; Mangala, L. S.; Han, H. D.; Lu, C.; Bottsford-Miller, J.; Nishimura, M.; Mora, E. M.; Lee, J. W.; Stone, R. L.; Pecot, C. V.; *et al.* Targeted Delivery of Small Interfering Rna Using Reconstituted High-Density Lipoprotein Nanoparticles. *Neoplasia* **2011**, *13*, 309–319.
54. Rui, M.; Tang, H.; Li, Y.; Wei, X.; Xu, Y. Recombinant High Density Lipoprotein Nanoparticles for Target-Specific Delivery of Sirna. *Pharm. Res.* **2013**, *30*, 1203–1214.
55. McConathy, W. J.; Nair, M. P.; Paranjape, S.; Mooberry, L.; Lacko, A. G. Evaluation of Synthetic/Reconstituted High-Density Lipoproteins as Delivery Vehicles for Paclitaxel. *Anti-Cancer Drugs* **2008**, *19*, 183–188.
56. Yang, M.; Chen, J.; Cao, W.; Ding, L.; Ng, K. K.; Jin, H.; Zhang, Z.; Zheng, G. Attenuation of Nontargeted Cell-Kill Using a High-Density Lipoprotein-Mimicking Peptide−Phospholipid Nanoscaffold. *Nanomedicine* **2011**, *6*, 631–641.
57. Duivenvoorden, R.; Tang, J.; Cormode, D. P.; Mieszawska, A. J.; Izquierdo-Garcia, D.; Ozcan, C.; Otten, M. J.; Zaidi, N.; Lobatto, M. E.; van Rijs, S. M.; *et al.* A Statin-Loaded Reconstituted High-Density Lipoprotein Nanoparticle Inhibits Atherosclerotic Plaque Inflammation. *Nat. Commun.* **2014**, *5*, 3065.
58. Jin, C. S.; Cui, L.; Wang, F.; Chen, J.; Zheng, G. Targeting-Triggered Porphysome Nanostructure Disruption for Activatable Photodynamic Therapy. *Adv. Healthcare Mater.* **2014**, *3*, 1240–1249.

59. Perrault, S. D.; Walkey, C.; Jennings, T.; Fischer, H. C.; Chan, W. C. Mediating Tumor Targeting Efficiency of Nanoparticles through Design. *Nano Lett.* **2009**, *9*, 1909–1915.
60. Cabral, H.; Matsumoto, Y.; Mizuno, K.; Chen, Q.; Murakami, M.; Kimura, M.; Terada, Y.; Kano, M. R.; Miyazono, K.; Uesaka, M.; Nishiyama, N.; Kataoka, K. Accumulation of Sub-100 nm Polymeric Micelles in Poorly Permeable Tumours Depends on Size. *Nat. Nanotechnol.* **2011**, *6*, 815–823.
61. Yuan, F.; Leunig, M.; Huang, S. K.; Berk, D. A.; Papahadjopoulos, D.; Jain, R. K. Microvascular Permeability and Interstitial Penetration of Sterically Stabilized (Stealth) Liposomes in a Human Tumor Xenograft. *Cancer Res.* **1994**, *54*, 3352–3356.
62. Davis, M. E.; Chen, Z. G.; Shin, D. M. Nanoparticle Therapeutics: An Emerging Treatment Modality for Cancer. *Nat. Rev. Drug Discovery* **2008**, *7*, 771–782.
63. Cheng, L.; Wang, C.; Feng, L.; Yang, K.; Liu, Z. Functional Nanomaterials for Phototherapies of Cancer. *Chem. Rev.* **2014**, *114*, 10869–10939.
64. Chapman, M. J. Animal Lipoproteins: Chemistry, Structure, and Comparative Aspects. *J. Lipid Res.* **1980**, *21*, 789–853.
65. Liu, T. W.; MacDonald, T.; Shi, J.; Wilson, B. C.; Zheng, G. Intrinsically Copper-64-Labeled Organic Nanoparticles as Radiotracers. *Angew. Chem., Int. Ed. Engl.* **2012**, *51*, 1–5.